Journal of Electroanalytical Chemistry 1003 (2026) 119801

Contents lists available at ScienceDirect

Journal of Electroanalytical Chemistry

journal homepage: www.elsevier.com/locate/jelechem

Chemometrically optimized electrochemical decoupling of the uric acid–xanthine purine pair via single-step co-synthesized composite

Nguyen Minh Quang [a], Do Mai Nguyen [b], Vo Chau Ngoc Anh [c], Tran Thanh Tam Toan [d,*], Anh-Quang Dao [e,f,**]

[a] Faculty of Chemical Engineering, Industrial University of Ho Chi Minh City, Ho Chi Minh City, 700000, Viet Nam
[b] University of Sciences, Hue University, Hue city, 530000, Viet Nam
[c] University of Medicine and Pharmacy, Hue University, 530000, Viet Nam
[d] Dong A University, Danang city 550000, Viet Nam
[e] Faculty of Environmental and Natural Sciences, Duy Tan University, Da Nang 550000, Viet Nam
[f] Institute of Research and Development, Duy Tan University, Da Nang 550000, Viet Nam

ARTICLE INFO

Keywords:
Electrochemical decoupling
Chemometrics
Uric acid and xanthine
Single-step co-synthesis
Poly(bromocresol purple)-RGO

ABSTRACT

An electrochemical sensor was developed with a modified glassy carbon electrode (GCE) by a poly(bromocresol purple) (PBSP) and electrochemically reduced graphene oxide (RGO) composite. The modified electrode was prepared via a single-step electrochemical co-deposition technique, which represents a methodological refinement aimed at enhancing the simplicity and structural integration of the components. The resulting PBSP-RGO/GCE-modified electrode was evaluated for the dual electrochemical detection of uric acid (URC) and xanthine (XAT). An analytical improvement was achieved as the oxidation electrochemical signals of these two urinary metabolites were clearly resolved, reducing the problem of signal overlap commonly encountered in conventional sensing platforms. The observed enhancement in electrochemical activity is due to the combination of the high electrical conductivity of the RGO support and the functional selectivity imparted by the PBSP polymer layer. The sensor demonstrated good sensitivity and low limits of detection (LODs) for both analytes, with URC being reliably determined in a wide linear concentration range. Furthermore, the actual sample investigation of the technique was indicated through the analysis of real biological matrices (urine), where recovery rates ranging from 96 % to 105 % were consistently documented. The findings were statistically confirmed to be in comparison with the standard high-performance liquid chromatography (HPLC) technique, establishing the accuracy and reliability of the proposed sensor.

1. Introduction

Altered levels of uric acid (URC) and xanthine (XAT), terminal purine metabolites, have been linked in recent years to a growing cardiometabolic and renal burden beyond gout alone. Global estimates now indicate rising prevalence and years lived with disability (YLDs) symptoms for gout through 2050, which has kept URC monitoring squarely on the clinical agenda. Mechanistic and translational studies have also identified xanthine oxidoreductase (XOR) as a driver of reactive oxygen species (known as ROS) and endothelial dysfunction, indicating the value of tracking purine metabolites together [1–6].

From an exposure perspective, URC in biofluids reflects endogenous purine turnover but is also influenced by exogenous inputs. Dietary patterns rich in animal-based purines and sugar-sweetened beverages have been associated with higher urate levels, whereas plant-forward patterns correlate inversely with the risk of hyperuricemia. National databases now provide updated food-specific purine contents, and some guidelines recommend limiting daily purine intake (e.g., $\leq$ 400 mg day^{-1} in Japan) [4,7–9]. Beyond clinical matrices (serum, urine, saliva), purine degradation products accumulate in foods during storage. Specifically, inosine/IMP decays to HPX (hypoxanthine) and then to XAT, which are widely used as freshness indices in fisheries (K-value) and have been quantified recently by HPLC/UV. These trends indicate the analytical relevance of URC/XAT across biomedical testing and food-

* Corresponding author.
** Corresponding author at: Faculty of Environmental and Natural Sciences, Duy Tan University, Da Nang 550000, Viet Nam.
E-mail addresses: toanttt@donga.edu.vn (T.T.T. Toan), daoanhquang@duytan.edu.vn (A.-Q. Dao).

https://doi.org/10.1016/j.jelechem.2026.119801
Received 26 October 2025; Received in revised form 21 December 2025; Accepted 4 January 2026
Available online 6 January 2026

quality monitoring [10,11].

Against this broad need, enzymatic spectrophotometry (uricase, often single-analyte), chromatography (high-performance liquid chromatography-UV–Vis/HPLC-UV or liquid chromatography-mass spectrometry LC–MS), and capillary electrophoresis have provided specificity but at the expense of cost, instrumentation, and throughput. Electrochemical methods have therefore been pursued for rapid, low-volume analyses; however, on bare glassy carbon electrodes (GCE), URC and XAT oxidize in a narrow potential scan and their products can foul the surface, compromising resolution and stability in bio-like matrices [12–14].

To address these issues, graphene-based interfaces have been widely investigated. Reduced graphene oxide (denoted as RGO) provides high electrochemical surface area and conductivity and, importantly, can be formed directly on electrodes by electrochemical reduction of drop-cast GO (graphene oxide) in water—an approach described as "green" because electrons serve as the reductant and film thickness is tuned in situ. Despite these advantages, RGO alone has not consistently delivered baseline separation or long-term antifouling for URC/XAT, motivating the addition of functional overlayers [15–17].

Electropolymerized sulfonephthalein dyes provide such an overlayer under similarly mild conditions. Bromocresol purple (BSP) can be anodically polymerized to yield conjugated, electroactive PBSP (poly (bromocresol purple)) films. On GCE, PBSP alone has enabled the simultaneous voltammetric determination of URC, XAT, and HPX, indicating intrinsic catalytic/affinity interactions with purines. When integrated with conductive carbons or nanoparticles, further decreases in charge-transfer resistance and higher faradaic currents have been reported [18–20]. In parallel, green PBSP/graphene composites have been prepared and validated electrochemically for small phenolics, establishing feasibility for dye–graphene hybrids produced without hazardous chemical reductants [21].

These strands motivate the present strategy: a PBSP–RGO film assembled *entirely in aqueous media* by a sequential, electrode-driven route—(i) drop-casting GO on GCE, (ii) electrochemical reduction to RGO, and (iii) cyclic voltammetry (CV) electropolymerization of BSP—followed by CV and differential pulse voltammetry (DPV) for URC/XAT. The rationale is that the RGO backbone will expedite electron transfer and enlarge the active area, while the PBSP overlayer will provide π–π/electrostatic affinity and mitigate passivation. This design is informed by prior successes of RGO-based dual-purine sensors (with *other* polymers) and of PBSP films (without graphene) for URC/XAT/HPX, but—to the best of knowledge—its specific confluence as a fully aqueous, sequentially electrosynthesized PBSP–RGO interface targeted at simultaneous URC/XAT remains scarcely reported [13,14,18,22].

The intended contributions are therefore threefold—articulated with appropriate caution. First, a green synthesis is implemented for both constituents (RGO by electroreduction; PBSP by CV polymerization), minimizing reagents and waste while affording adhesion and thickness control. Second, a complementary interface is created in which conductivity/area (RGO) and affinity/antifouling (PBSP) are combined to pursue clearer URC/XAT baseline separation and reduced drift over repeated scans. Third, analytical relevance is examined not only in buffer but also in bio-like contexts (and, by extension, in food matrices where XAT/HPX accumulate), situating the work among recent efforts on simultaneous purine sensing with engineered carbon–polymer hybrids.

Motivated by these considerations, a PBSP–RGO film was assembled entirely in aqueous media by a sequential, electrode-driven route—(i) drop-casting GO on polished GCE, (ii) electrochemical reduction to RGO, and (iii) CV electropolymerization of BSP to form a conformal π-rich overlayer. The working hypothesis was that the RGO backbone would expedite electron transfer and enlarge the active area. In contrast, the PBSP overlayer would confer π–π/electrostatic affinity and antifouling behavior, thereby improving peak resolution and analytical figures of merit for URC and XAT under CV/DPV. As far as could be determined, reports explicitly combining on-electrode RGO formation with in-situ PBSP growth for simultaneous URC/XAT determination via a fully aqueous workflow have remained scarce.

2. Experimental

2.1. Chemicals

All employed reagents were obtained from Merck (Germany), verified at ≥99 % purity, and applied as received with no further purification. Uric acid (URC) and xanthine (XAT) were employed as target standards, and hypoxanthine (HPX) was included for selectivity assessments. Bromocresol purple (BSP) was electropolymerized to form a poly(bromocresol purple) (PBSP) film. Graphene oxide was modified by drop-casting on GCE and electrochemically in situ to reduced graphene oxide (RGO). Potassium nitrate (KNO_3) was used as the supporting electrolyte during BSP electropolymerization. A phosphate buffer (PBS, 0.2 M; pH 3.0–8.0) was prepared from NaH_2PO_4 and Na_2HPO_4 and used for electrode conditioning and voltammetric measurements. Ascorbic acid, paracetamol (acetaminophen), clenbuterol (HCl salt where applicable), ammonium sulfate ($(NH_4)_2SO_4$), ferric chloride ($FeCl_3$), sodium chloride (NaCl) and calcium nitrate ($Ca(NO_3)_2$).

2.2. Instruments

Fourier-transform infrared spectra were described using a Shimadzu IR Prestige 21 (Japan). The Raman spectra measurements were applied on an XPLORA, HORIBA instrument utilizing a 532 nm laser.

Voltammetry tests were carried out using a Autolab/PGSTAT101 configured with a 3-electrode system. A glassy carbon electrode (GCE), measuring 2.80 ± 0.1 mm in diameter, was utilized to construct the modified-based working electrode (WE). An Ag/AgCl/3.0 M KCl electrode was applied as the reference electrode and a platinum (Pt) wire was employed as the auxiliary electrode.

Comparative analyses of the analytes were carried out using a Thermo Ultimate 3000 UHPLC (ultra-high-performance liquid chromatography) system. The chromatographic parameters applied included a column temperature maintained at 45.0 °C ± 1.0 °C, a flow rate set at 2.0 mL/min, and an injection volume of 10.0 μL. Tests were achieved using a UV detector operating at a wavelength of $\lambda = 275$ nm. Quantitative calculations were performed using external standardization based on the measurement of peak areas from the chromatograms.

2.3. The preparation of PBSP-RGO/GCE

A glassy carbon electrode (GCE) was first mirror-polished on 0.3 μm and 0.05 μm alumina slurries microcloth, followed by sequential ultrasonication in ethanol and ultrapure water (3 min each) and gentle drying under nitrogen. This routine was adopted to minimize residual surface oxides and debris before film assembly.

RGO was then grown in situ by electrochemical reduction of a cast GO dispersion, to avoid chemical reductants, to maintain an environmentally friendly fabrication process. Aqueous GO (typically 0.5–1.0 mg mL^{-1}) was dropped-cast (3–5 μL) onto the cleaned GCE and air-dried. The coated electrode was immersed in neutral PBS (0.1 M, pH 7.0), and the GO overlayer was electro-reduced by CV, tested range from −1.5 V and + 1.50 V until a stable voltammetric signature indicative of RGO formation was observed; this potential range has been widely used to convert GO to electrochemically RGO on carbon substrates [23]. To contextualize this choice, electrochemical reduction of cast GO films is a well-established, reagent-free approach that affords conformal RGO coatings and improved charge-transfer properties, with numerous studies showing comparable ranges or constant-potential steps spanning −0.6 to −1.5 V [24,25].

Upon obtaining the RGO underlayer, a sulfonephthalein dye was electropolymerized to yield the PBSP overlayer directly on RGO/GCE. In

line with prior work on poly(sulfonephthalein) films, BSP, a representative sulfonephthalein monomer, was selected as the benchmark electrolyte formulation because its electro-oxidative polymerization is reliable and well established. Polymerization was applied in 2.0 mM BSP prepared in 0.1 M KNO_3, using CV across a wide potential range that spans the dye's redox transitions (from −1.50 V to +1.50 V) until the characteristic growth and stabilization of the film currents were achieved. The same electrolyte and CV's potential range have been used to form PBSP films on carbon nanostructured substrates, providing reproducible coverage and high electrocatalytic activity [19]. For completeness, the electropolymerization of sulfonephthalein dyes on conductive carbon supports has also been demonstrated on related architectures (e.g., carbon nanotube CNT/GCE), further supporting the chosen chemistry and sequence [20].

After polymer growth, the electrode was rinsed thoroughly with water and conditioned by potential cycling in a supporting electrolyte solution (0.2 M PBS buffer, pH 7.0) over a narrow, application-relevant range to remove loosely adsorbed monomer and to stabilize the PBSP–RGO interface before analytical measurements. The overall assembly electrochemically reduced process of GO and in situ electropolymerization of a sulfonephthalein is consistent with previous environmentally friendly composite-film methods that yield conductive scaffolds and functional molecular recognition layers [16,21].

Notes on reproducibility: RGO thickness and PBSP coverage were controlled by the number of CV cycles and monomer concentration, respectively; both parameters were maintained constant within a batch to ensure inter-electrode reproducibility. The chosen order (PBSP first, RGO second) was favored to combine the high electronic conductivity and adsorption capacity of RGO with the π–π/electrostatic affinity and antifouling character imparted by the poly(sulfonephthalein) overlayer, consistent with prior demonstrations of BSP-RGO assembly on GCE and its stability under repeated voltammetric operation [21].

2.4. The analysis of actual samples

To evaluate the proposed method, three voluntary human-tested urinary samples were acquired from a clinical lab. Various analytical purine samples were prepared in two ways: non-spiked and spiked.

For both sample types, an initial treatment procedure was employed to remove precipitates, which involved centrifugation at 4000 rpm for 20 min at 15 °C and filtering the obtained solution with a 0.45 μm diameter-membrane filter. In the specific case of spiked samples, known quantities of URC and XAT were added to the raw urine and mixed thoroughly before the aforementioned centrifugation and filtration steps were performed. Finally, the proposed DPV method was utilized to investigate the concentrations of URC and XAT in the treated sample solutions.

3. Results and discussions

3.1. The electrochemical reduction process of GO and BSP

Fig. 1a monitors the in situ synthesis process of the PBSP-RGO composite film on GCE. The formation of the composite was achieved via a simultaneous reaction pathway monitored through repeated potential cycling. The appearance of a distinct anodic peak at approximately +0.80 V is definitively attributed to the irreversible oxidation of the BSP monomer, which initiates the film formation. Concurrently, a cathodic peak observed at −1.21 V is confirmed, which indicates the simultaneous electrochemical reduction of the GO substrate to RGO alongside the reduction of the forming polymer. The confirmation of both processes within this single, strategically selected potential range illustrates the successful in situ fabrication of the PBSP-RGO composite. This single-step electrochemical route is advantageous as it effectively indicates the electrode assembly process while ensuring optimal integration between the conductive carbon scaffold and the functional polymer layer.

Fig. 1b was constructed to evaluate the efficacy of the various electrode interfaces for the simultaneous determination of URC and XAT. Initially, the bare GCE is observed to exhibit a weak current response with poorly resolved oxidation peaks, which establishes the necessity for surface modification. While modification with RGO/GCE results in a moderate enhancement of the signal, a phenomenon ascribed to the increased conductivity and surface area supplied by the RGO, baseline separation of the two analytes remains inadequate. In sharp contrast, the highest electrocatalytic activity and best resolution are demonstrated by the PBSP-RGO/GCE electrode. On this surface, an increase in the peak currents for both URC and XAT is observed. Most critically, the two oxidation signals are sharply resolved and shifted to significantly lower overpotentials when compared to the rest electrodes. This improved performance indicates that the incorporation of the PBSP layer onto the conductive RGO scaffold provides the necessary selectivity to minimize interference with the simultaneous determination of these purine metabolites. In addition, the separation is attributed to the distinct electrocatalytic environments provided by the PBSP-RGO interface. The RGO backbone expedites electron transfer, enhancing current response, while the PBSP overlayer modifies the surface adsorption thermodynamics, differentially shifting the oxidation potentials of URC and XAT

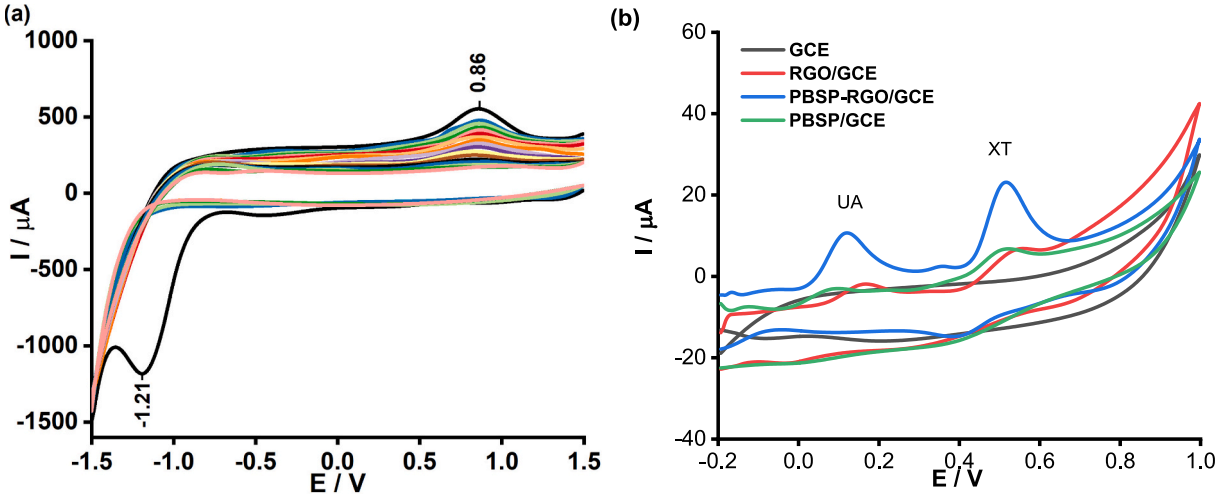

Fig. 1. (a) CVs for the simultaneous electropolymerization of BSP and electrochemical reduction of GO on a GO/GCE, (b) Comparative CVs showing the electrochemical responses of URC and XAT at various working electrodes.

to lower overpotentials and thereby increasing the peak separation to approximately 0.5 V.

3.2. The characterization of PBSP-RGO

Fig. 2a displays the Raman spectra for GO and the reduced product (RGO). Both materials exhibit the characteristic D-band (disorder) and G-band (sp^2 lattice). The structural transformation upon reduction is confirmed by a notable increase in the intensity ratio of the D-band to the G-band (I_D/I_G) from 0.92 for GO to 1.17 for RGO. This significant increase indicates the successful electrochemical reduction process, as it reflects the creation of new defects and a decline in the average size of sp^2 domains within the graphitic lattice. This controlled introduction of defects is essential for the material's application because these sites are known to serve as crucial centers that enhance electrochemical activity.

The FTIR spectra presented in Fig. 2b track the chemical transformation of the functional groups during the synthesis process. The original GO spectrum displayed prominent absorption peaks characteristic of oxygenation (e.g., broad O − H stretch at 3400 cm^{-1} and C═O stretch at 1718 cm^{-1}). Following electrochemical reduction, the RGO spectrum showed a systematic and significant diminution of the hydroxyl (O − H) stretching vibrations at 3400 cm^{-1} (phenolic O − H) and 1350 cm^{-1} (C − OH stretch). This indicates the successful removal of the majority of oxygen-including groups, which is critical for restoring the material's electrical conductivity. Concurrently, the final PBSP-RGO composite spectrum validates the successful grafting of the functional polymer network. New absorption bands are observed to intensify at 1110 cm^{-1} (C − O − C ether stretch) and 1245 cm^{-1} (C − O − S stretch). This illustrates that the PBSP layer was integrated onto the reduced graphene surface, providing chemical functionality for selective purine affinity.

3.3. Optimization of conditions for PBSP-RGO/GCE electrode fabrication for URC and XAT determination

The following parameters were utilized for the optimization of the PBSP-RGO/GCE electrode fabrication process via chemometric experimental design, considering three influencing factors (Table S1).

Experimental Conditions

- Potential range: The potential was scanned from −1.0 V and + 1.6 V. The scan was initiated from 0 V to prevent an initial potential shock.
- Electrolyte solution: BCP 2 mM prepared in a 0.2 M PBS at pH 5.0.
- Operating conditions: The experiment was conducted at room temperature (25 °C), in a mildly stirred solution.
- Electrode storage: The *WE* was rinsed with distilled water, followed by drying, and stored under a nitrogen (N_2) atmosphere.
- Experimental design Model: The experiment was executed using a chemometric model consisting of 3 center-point trials and 12 base-condition trials.

A three-factor, three-level Box–Behnken design (BBD) was implemented to map the quadratic response surface of Ip for URC and XAT while keeping the total number of experiments economical and estimation variance well-behaved near the design center. This choice is consistent with the canonical formulation of BBD introduced by Box and Behnken, in which factors are set at coded levels −1, 0 and + 1 to enable efficient estimation of linear, interaction and pure quadratic effects without corner points of the full cube. Second-order polynomial regression models with three variables were obtained from the experimental data using Minitab (Table S2).

$$I_{p,URA} = 6.153 + 0.4727\,A + 0.3619\,B + 0.07820\,C - 0.03936\,A^2 - 0.008779\,B^2 - 0.0003679\,C^2 + 0.00032\,A^*B - 0.000097\,A^*C + 0.000030\,B^*C$$

$$(R^2 = 0.997,\ R_a^2 = 0.991,\ R_{pred}^2 = 0.951)$$

$$I_{p,XAT} = 9.867 + 0.5047\,A + 0.4190\,B + 0.05795\,C - 0.04705\,A^2 - 0.011679\,B^2 - 0.0003454\,C^2 + 0.00179\,A^*B + 0.000208\,A^*C + 0.0003066\,B^*C$$

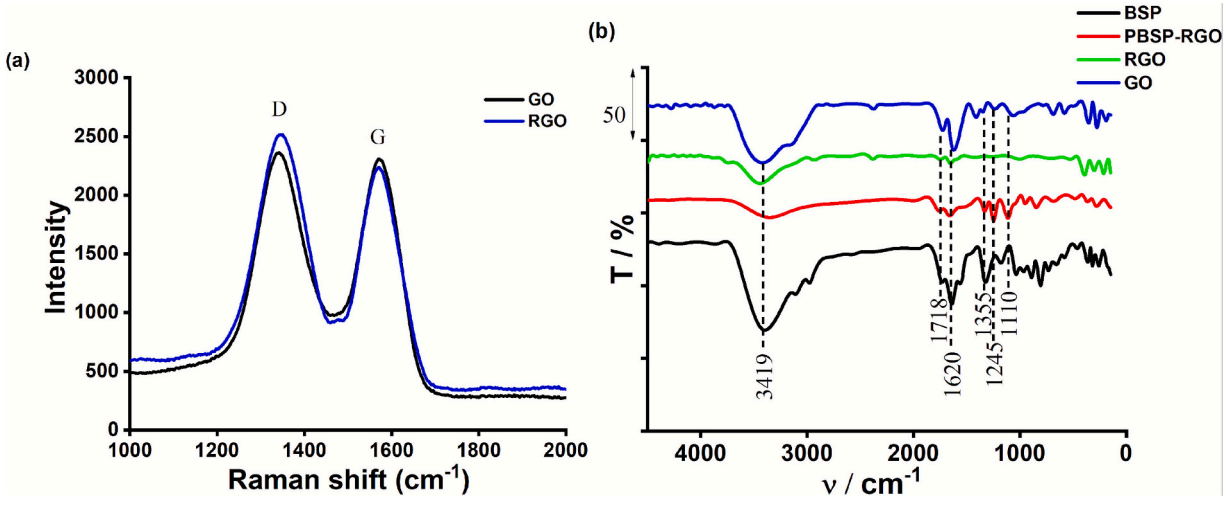

Fig. 2. (a) Raman spectra of GO and RGO, (b) FTIR spectra of BSP, PBSP-RGO, RGO, and GO.

($R^2 = 0.999$, $R_a^2 = 0.996$, $R_{pred}^2 = 0.992$)

A second-order polynomial model was fitted to Ip for each analyte. Excellent model adequacy was indicated by URC: $R^2 = 0.997$, $R^2_{adj} = 0.991$, $R^2_{pred} = 0.951$ and XAT: $R^2 = 0.999$, $R^2_{adj} = 0.996$, $R^2_{pred} = 0.992$. Analysis of variance showed that all main effects (A, B, C) and all quadratic terms (A,[2] B^2, C^2) were highly significant ($p < 0.0001$). In contrast, two-factor interactions were generally negligible except for the B × C term, which reached significance for XAT ($p = 0.0259$). Lack-of-fit was not significant for either response, supporting the sufficiency of the quadratic model within the explored domain. These results are fully consistent with the expected curvature-dominated landscapes typically obtained with BBD in electrochemical sensor optimization.

Model adequacy and the statistical significance of individual terms were evaluated by analysis of variance (ANOVA) for the quadratic response-surface models of Ip, URC and Ip, XAT. The results are summarized in Table S3.

Significant overall models were obtained for both responses (Model, $F > 1$, $p < 0.0001$), confirming that the second-order polynomials captured the dominant variability in the BBD data. For each analyte, the three main effects—GO amount (A), number of scans (B), and scan rate (C)—were significant at $p < 0.0001$, and all quadratic terms (A,[2] B^2, C^2) were significant, evidencing pronounced curvature. Two-factor interactions were negligible for URC (AB, AC, BC; $p \geq 0.05$), whereas a modest B × C interaction reached significance for XAT ($p = 0.0259$), indicating that the effect of scan rate became contingent on film-growth cycles. The lack-of-fit term was not significant, in agreement with the high R,[2] R^2_{adj}, and R^2_{pred} values reported for the fitted equations, and supporting the sufficiency of the quadratic models within the explored factor space.

To visualize these effects and the inferred curvature, response surface plots were inspected, as shown in Fig. 3. For both analytes, dome-shaped surfaces were observed, consistent with significant quadratic terms: I_p increased with the number of scans (B) and with the scan rate (C) from their low levels and then decreased after passing a curvature-bounded maximum. The influence of the GO loading (Factor A), which serves as a determinant for the thickness of the generated RGO film, was analyzed. It was observed that this factor exhibited a non-monotonic influence on the peak currents. This behavior is interpreted as a balance between the beneficial expansion of the electroactive surface area provided by the RGO scaffold at moderate loadings and the detrimental effects associated with excessive film thickness. Specifically, at higher loadings, the increased film thickness is suggested to introduce greater electron transfer resistance and hinder the mass transport of analytes to the electrode surface, thereby diminishing the electrochemical signal. In the XAT maps, slightly stronger warping was noted in the B—C plane, in agreement with the significant B × C term from ANOVA. The stationary region common to both responses was centered near A ≈ 6 μg, B ≈ 20 scans, and C ≈ 100 mV s^{-1}, which guided the subsequent desirability-based search for operating conditions and the confirmation experiments.

Guided by the ANOVA results, reduced second-order models were refitted by retaining only statistically significant coefficients ($p < 0.05$); these predictive equations were subsequently used for desirability-based optimization.

From the above evaluation, the regression equation with significant coefficients was reduced as follows:

$$I_{p,URA} = 6.153 + 0.4727\,A + 0.3619\,B + 0.07820\,C - 0.03936\,A^2 - 0.008779\,B^2 - 0.0003679\,C^2$$

$$I_{p,XAT} = 9.867 + 0.5047\,A + 0.4190\,B + 0.05795\,C - 0.04705\,A^2 - 0.011679\,B^2 - 0.0003454\,C^2 + 0.0003066\,B^*C$$

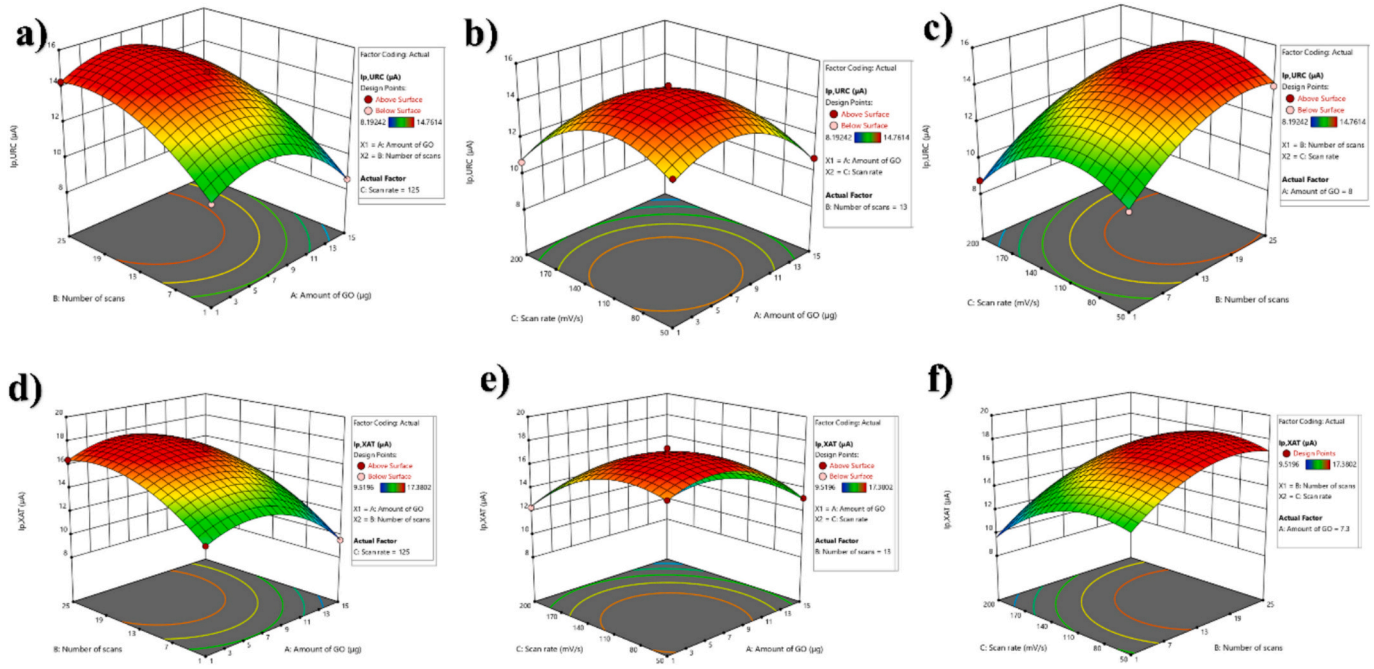

Fig. 3. Response surface plots showing the effect of (a) GO amount and number of scans, (b) GO amount and scan rate, and (c) number of scans and scan rate on I_p of URC; and (d–f) the corresponding effects on I_p of XAT.

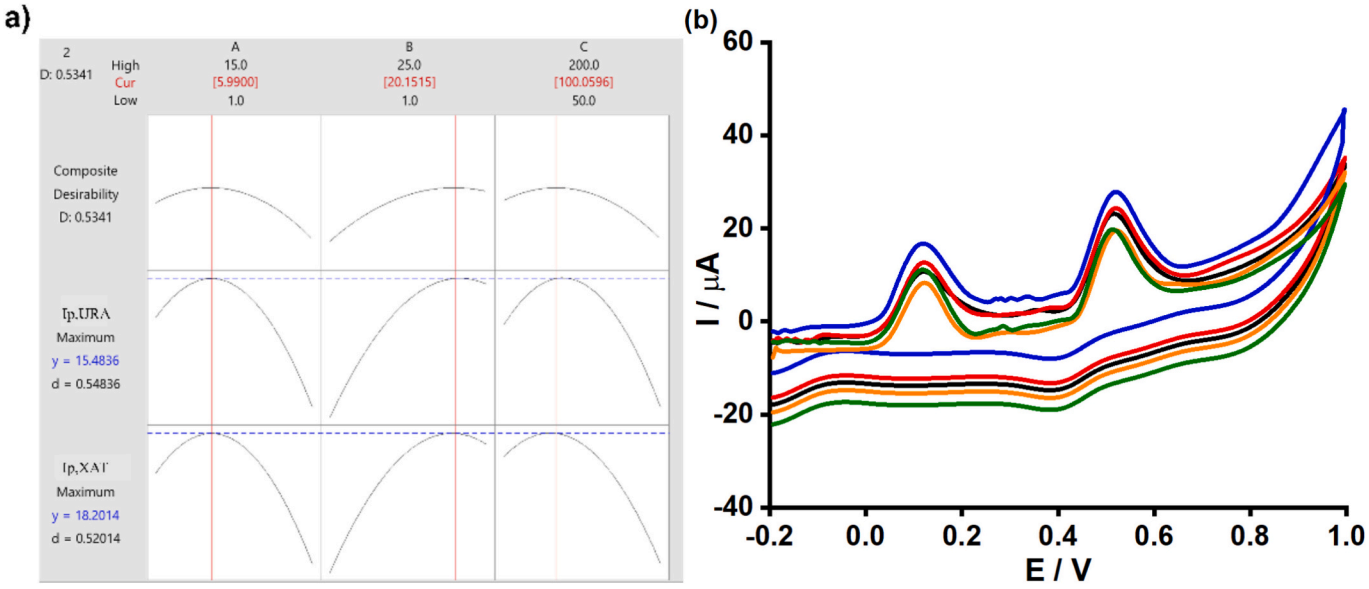

Fig. 4. (a) Composite desirability profiles at the optimal point; (b) CVs of URC and XAT recorded at the optimum.

Table 1
Predicted optimal conditions and Ip of URC and XAT at the optimum.

Predicted optimal conditions			Predicted peak current at the optimum		Experimental peak current at the optimum	
Amount of GO (µg)	Number of scans	Scan rate (mV s^{-1})	$I_{p,\ URC}$ (µA)	$I_{p,XAT}$ (µA)	$I_{p,\ URC}$ (µA)	$I_{p,XAT}$ (µA)
~6.0	20	100	15.48	18.20	15.12 ± 0.39(*)	18.03 ± 0.34(*)

(*) *Mean ± SD (n = 5).*

Guided by the reduced quadratic models, a composite desirability approach was applied to identify the operating point that simultaneously maximizes I_p for both analytes; the predicted optimum and confirmation CVs are shown in Fig. 4. A composite desirability of ~0.53 was achieved at GO ≈ 6.0 µg, 20 scans, and 100 mV s^{-1}. Under these settings, the models predicted $I_{p,\ URC} = 15.48$ µA and $I_{p,\ XAT} = 18.20$ µA (Fig. 4a). As depicted in the prediction profile in Fig. 4a (specifically in the column for Factor A), the peak currents for both URC and XAT are observed to increase as the GO loading rises from the lower level (1.0 µg) to the approximate optimum (≈ 6.0 µg), followed by a gradual decline upon further increment. This trend is interpreted as an initial enhancement of electrode activity due to the increased surface area provided by the graphene scaffold; however, beyond the optimal point, the excessive accumulation of GO results in a thicker film, which is suggested to hinder the electron transfer process across the modifier layer. The CVs recorded at the optimum (Fig. 4b) displayed amplified and well-resolved anodic responses for both analytes, consistent with the curvature inferred from the response-surface maps. These conditions were therefore carried forward for quantitative evaluation.

The predicted operating point and the corresponding experimental verification are reported in Table 1. Experimental peak currents of 15.12 ± 0.39 µA (URC) and 18.03 ± 0.34 µA (XAT) (mean ± SD, $n = 5$) were obtained at the predicted optimum, closely matching the model outputs (15.48 and 18.20 µA, respectively). No statistically significant deviations from prediction were detected by *t*-tests, thereby validating the predictive adequacy of the reduced quadratic models and confirming the suitability of the selected operating conditions for subsequent analytical studies. With the operating point validated, calibration characteristics and limits of detection were established by CV and DPV under these optimized conditions.

3.4. *The determination of URC and XAT by PBSP-RGO/GCE.*

3.4.1. *Cyclic voltammetry*

The impact of pH on the electrochemical response of URC and XAT at the PBSP-RGO/GCE was systematically investigated, with the results displayed in Fig. 5a and b. As shown in the CVs in Fig. 5a, the oxidation peak potentials (*Ep*) for both URC and XAT were observed to shift negatively as the pH was increased from 3.0 to 8.0. This behavior is consistent with protons are involved in the electrode reaction mechanism of both molecules.

The corresponding plot of peak current (*Ip*) versus pH is shown in Fig. 5c. For both URC and XAT, the anodic peak currents were found to rise with pH, reaching a highest value at pH 7.0, and subsequently dropping at higher pH levels. This trend indicates that a neutral environment provides the optimal conditions for the electro-oxidation of these purine bases. Therefore, pH 7.0 was chosen for the next analytical experiments to achieve the highest possible sensitivity.

To further evaluate the modified electrode reaction mechanism, the plot between the peak potential (*Ep*) and pH was examined, as presented in Fig. 5d. A linear correlation was found for both URC and XAT over the pH range studied. The linear regression equations were calculated as:

$E_{p.URC}$ (V) = (−0.061 ± 0.006)pH + (0.597 ± 0.034); $R^2 = 0.991$.

$E_{p.XAT}$ (V) = (−0.059 ± 0.003)pH + (1.003 ± 0.018) $R^2 = 0.988$.

The slopes of −0.061 for URC and − 0.059 for XAT are in close agreement with the theoretical Nernstian value of −0.059. This result indicates that the electrochemical oxidation of both URC and XAT at the PBSP-RGO/GCE surface is a procedure with an equal number of protons and electrons. The proposed oxidation mechanism of URC and XAT is shown in Scheme 1. The observed enhancement in selectivity is attributed to the synergistic combination of the high electrical conductivity of the RGO support and the functional selectivity imparted by the PBSP polymer layer. While the specific molecular interactions, postulated to be a combination of π-π stacking between the purine rings and the polymer backbone, and electrostatic effects, were not isolated spectroscopically in this study, this hypothesis is consistent with the known affinity of electropolymerized dyes for purine bases. The primary focus remains on the achieved analytical resolution via the green synthesis

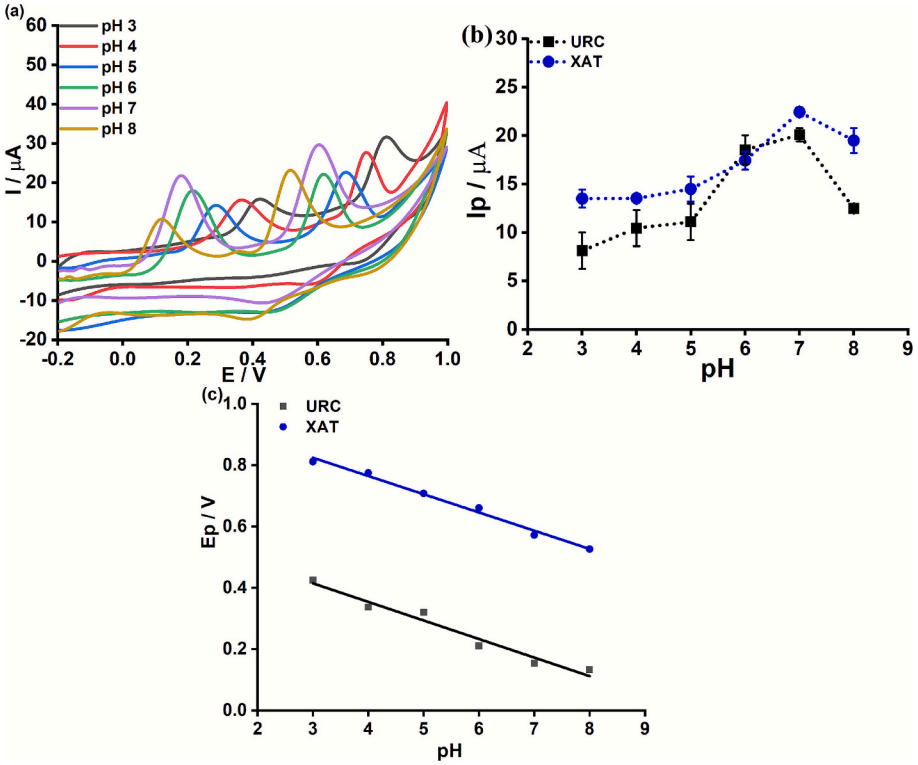

Fig. 5. (a) CVs of URC and XAT at pH 3.0–8.0; (b) The linear plot between *Ip* vs. pH (*n* = 3); (c) The plotting *Ep* versus pH (n = 3).

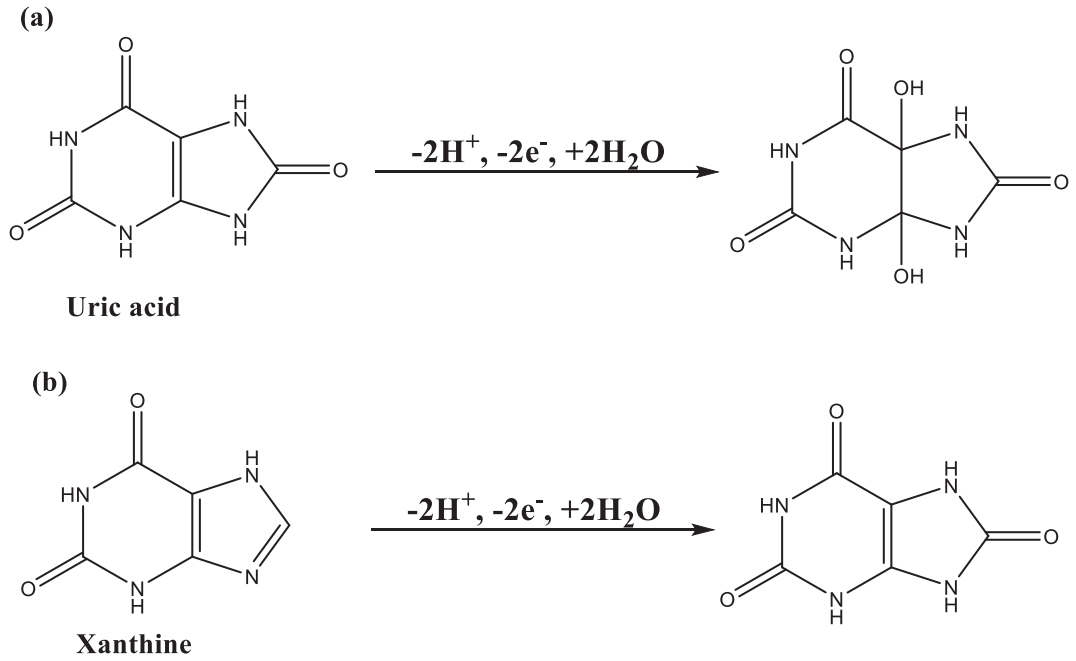

Scheme 1. The proposed mechanism for the URC (a) and XAT (b) oxidation [36, 37].

route. These results are highly consistent with recent findings in the field of purine electrochemistry [36, 37].

3.4.2. Differential pulse voltammetry.

- Linear range and limit of detection.

The DPV responses for varying concentrations of URC from 0.01 to 2.32 μM in the presence of a fixed concentration of XAT (0.2 μM) are presented in Fig. 6a. A well-defined oxidation peak corresponding to URC was observed to increase linearly with its concentration. This relationship is quantitatively represented in the calibration plot shown in Fig. 6b. A linear plotting between the peak current (*Ip*, URC) and concentration (C_{URC}) was established and is mathematically described by the regression eq. (4):

$$I_{p.URC}\ (\mu A) = (-0.14 \pm 0.03) + (41.72 \pm 0.50).C_{URC}\ (\mu M)\ R^2 = 0.998$$

A similar procedure was conducted for determining XAT with a fixed

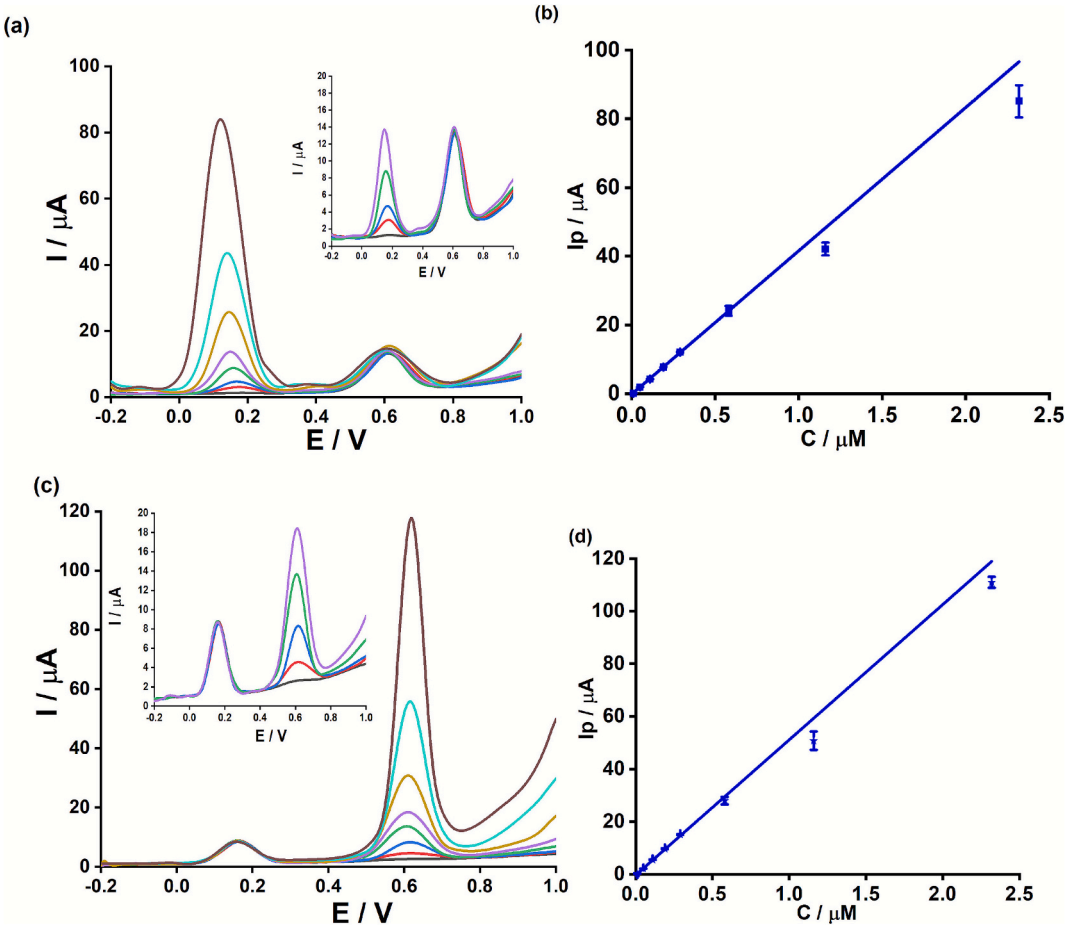

Fig. 6. (a) DPVs of URC with the rising of concentration from 0.01 to 2.32 µM and a certain concentration of XAT at 0.2 µM with the modified PBSP-RGO/GCE, (b) The plot of *Ip* vs. C_{URC} ($n = 3$), (c) DPVs of XAT with the increase of concentration from 0.01 to 2.32 µM and a certain concentration of URC at 0.2 µM with the modified PBSP-RGO/GCE, (d) The plotting of *Ip* vs. C_{XAT} (n = 3).

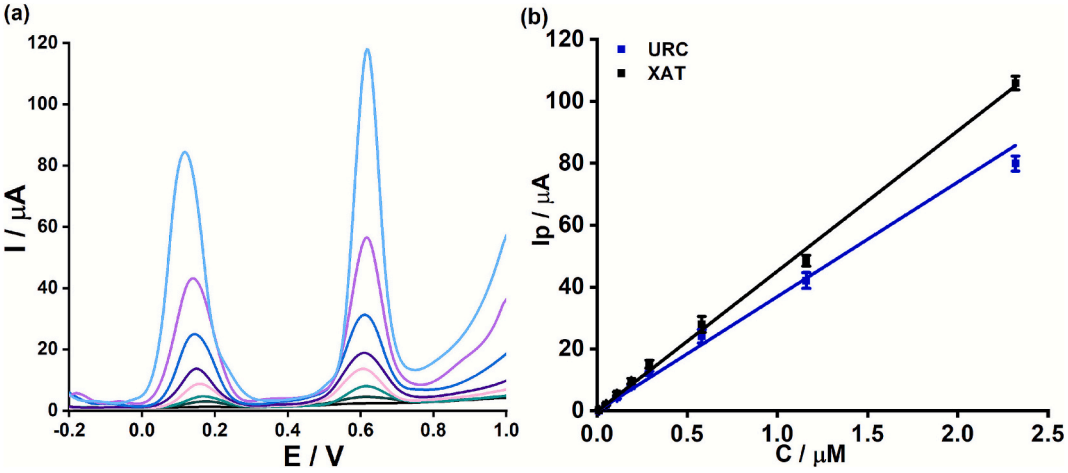

Fig. 7. (a) DPVs of URC and XAT at several concentrations from 0.01 to 2.32 µM with PBSP-RGO/GCE; (b) The plot of *Ip* versus $C_{URC,\ \mu M}$ and $C_{XAT,\ \mu M}$ ($n = 3$).

URC concentration, as shown in Fig. 6c. The resulting calibration curve in Fig. 6d also demonstrates excellent linearity. This linear response for XAT is described by the equation:

$$I_{p\ XAT}\ (\mu A) = (-0.30 \pm 0.02) + (51.41 \pm 1.01).C_{XAT}\ (\mu M)\ R^2 = 0.992$$

From the linear regression equations, the acquired LODs (3σ formula) were 0.008 µM and 0.005 µM for URC and XAT, respectively.

Experimental conditions: potential range − 0.2 V - +1.0 V, scan rate 0.2 V/s.

As shown in Fig. 7a, DPVs were recorded in solutions containing simultaneously increasing concentrations of both URC and XAT, ranging from 0.01 to 2.32 µM. Two distinct and well-resolved anodic peaks were observed at approximately +0.1 V and + 0.6 V for the oxidation of URC and XAT, respectively. The significant separation in peak potentials (0.5

Table 2
Reported analytical performance of URC/XAT electrochemical sensors.

Electrode material (*)	Analytes	Technique	Linear range (μM)	LOD (μM)	Ref.
NT Cu-MOF/CPE	URC XAT	DPV	0.25–75	0.1 0.25	[26]
CuO/N-Graphitic	URC XAT	DPV	50–1050 5–90	0.02 0.004	[27]
Co(*MOF*)TMA@CNF	URC XAT	Amperometry	25–700	0.1 0.1	[28]
$CaHPO_4.2H_2O$	URC XAT	DPV	1–433 1.5–420	0.6 1	[29]
Denser carbon fibers	URC XAT	DPV	30–1000 7–300	28.7 6.5	[30]
Nb(*BTC*)MOF@CNF	URC XAT	DPV	5–1200	0.07 0.08	[31]
3D GNP/rGO-CNT	URC XAT	SWV	1.56–25 3.13–25	0.91 2.57	[13]
PTA/CeO_2@Pt	URC XAT	DPV	8–434 10–330	0.0006 0.001	[32]
CoSe@B,N-IRPC	URC XAT	DPV	0.03–2587 0.01–4719	0.03 0.01	[33]
PBSP-RGO	URC XAT	DPV	0.01–2.32	0.009 0.007	This work

(*) CuO/N-Graphitic: Copper oxide/Nitrogen-Graphitic, Co(*MOF*)TMA@CNF: Co(*MOF*)trimesic acid@carbon nanofiber, Nb(*BTC*)MOF@CNF: Niobium(benzene benzene 1,3,5-tricarboxylic acid)MOF@carbon nanofiber, 3D GNP/rGO-CNT: 3D gold nanoparticle/reduced graphene oxide-carbon nanotube, PTA/CeO_2@Pt: polymer 3-amino-5-mercapto-1,2,4-triazole (PTA)/cerium dioxide (CeO_2) composite platinum (Pt), CoSe@B, N-IRPC: Cobalt selenide@boron, nitrogen co-doped interconnected reticulated porous carbon, PBSP-RGO: poly (bromocresol purple)-reduced graphene oxide.

V) is crucial, as it allows for the unambiguous identification and quantification of each analyte without mutual interference. It was observed that the peak currents for two analytes rise linearly with their respective concentrations.

This behavior is quantitatively illustrated by the calibration plots in Fig. 7b, where the peak currents (*Ip*) for URC and XAT are plotted against their concentrations. Excellent linear relationships were obtained for both species over the entire concentration range, reaffirming the sensor's suitability for simultaneous analysis.

$$I_{p.URC}\ (\mu A) = (-0.08 \pm 0.18) + (37.01 \pm 1.49).C_{URC}\ (\mu M)\ R^2 = 0.993 \quad (6)$$

$$I_{p.XAT}\ (\mu A) = (-0.18 \pm 0.14) + (45.33 \pm 1.09).C_{XAT}\ (\mu M)\ R^2 = 0.996 \quad (7)$$

The acquired LOD values for URC are 0.009 μM and for XAT are 0.007 μM (3σ formula), while the detected LOQ for URC and XAT are 0.03 μM and 0.02 μM. The sensitivity sensor value for URC and XAT is 37 μA/μM and 45 μA/μM, indicating their high responsiveness to targeted analytes with the concentration range 0.01 μM - 2.32 μM. The limits of detection (LODs) for URC and XAT were found to be highly consistent between individual (0.008 μM for URC, 0.005 μM for XAT) and simultaneous (0.009 μM for URC, 0.007 μM for XAT) determination experiments. This close agreement indicates minimal cross-interference between the two analytes, confirming that the PBSP-RGO/GCE sensor is reliable and effective for their simultaneous and sensitive quantification.

A detailed comparison of the developed analytical method with previously published electrochemical sensors is presented in Table 2. This evaluation is necessary to place the results in context with the performance of the PBSP-RGO/GCE electrode and confirm its potential utility within the landscape of purine metabolite detection. The principal figures of merit, specifically the limit of detection (LOD) and the linear working range (LR), are compared against various modified electrodes that have been reported for the determination of uric acid (URC) and xanthine (XAT). The analytical figures of merit achieved by the proposed PBSP-RGO/GCE sensor are observed to be generally competitive and comparable to those reported by other advanced electrochemical platforms. For the determination of URC and XAT, the attained LOD and the breadth of the linear range are shown to fall well within the performance envelope established by systems utilizing complex materials such as metal oxides, highly functionalized polymers, and other carbon nanomaterial composites.

However, the main difference lies in how these comparable metrics were achieved. In contrast to many reference methods that require sophisticated material synthesis or post-modification steps (e.g., using chemical reductants or long thermal treatments), the PBSP-RGO/GCE was fabricated via a simple, single-step electrochemical process. This in situ approach effectively simplifies the electrode preparation, leading to a highly integrated structure while simultaneously achieving the reduction of GO and the electropolymerization of the functional PBSP layer. Furthermore, the demonstrated ability of this electrode to achieve good resolution between URC and XAT at highly proximate potential regions, which is often a challenge even for advanced sensors, points to a subtle but significant analytical advantage. In conclusion, it is established that the proposed sensor, while yielding quantitative performance metrics that are similar to those of previously validated methods, offers a more accessible, time-efficient, and easily reproducible fabrication protocol. The high sensitivity achieved is maintained without recourse to high-cost or complicated synthesis routes, thereby positioning this developed method as a reliable and practical alternative for routine electrochemical analysis.

Experimental conditions: potential range from −0.2 V to +1.0 V, scan rate 0.2 V/s.

3.4.3. Interference

To investigate the practical applicability of the proposed sensor, its selectivity was evaluated by performing an anti-interference study. The influence of several common organic molecules and inorganic ions on the determination of URC and XAT was examined, with the results summarized in Table 3. Interferents were added at fixed molar ratios relative to the targets. Acceptance was defined a priori as a relative error within ±5 %. These potential interfering species were introduced into the analytical solution at concentration levels substantially higher than those of the target analytes.

It was observed that the relative error (*RE*) in the analytical signal for both URC and XAT remained within the range of −4.1 % to +4.7 %. As these deviations fall within the generally accepted analytical margin of ±5 %, it is described that the tested species do not impart a significant interference effect on the sensor's response. These findings indicate that the PBSP-RGO/GCE possesses a satisfactory anti-interference capacity and adequate selectivity, strengthening its potential for reliable application in the analysis of more complex samples.

3.4.4. Repeatability, reproducibility, long-term stability

3.4.4.1. Repeatability and reproducibility. To assess the consistency of the PBSP-RGO/GCE, a repeatability study was conducted at three distinct concentration levels of URC and XAT (0.1 μM, 0.19 μM, and

Table 3
Investigation of the effect of potential interfering species on the analytical signals of URC and XAT at the PBSP-RGO/GCE.

Interference	URC		XAT	
	$C_{interference}$:C_{URC}	*RE* (%)	$C_{interference}$:C_{XAT}	*RE* (%)
Hypoxanthine	120	4.1	50	−3.5
Clenbuterol	100	1.8	40	4.4
Ascorbic acid	30	2.9	190	−2.0
Paracetamol	190	4.7	30	3.4
$(NH_4)_2SO_4$	100	−2.4	50	−4.1
NaCl	80	−0.6	40	−3.8
$FeCl_3$	200	4.1	50	−3.9
$Ca(NO_3)_2$	120	−3.3	50	1.7

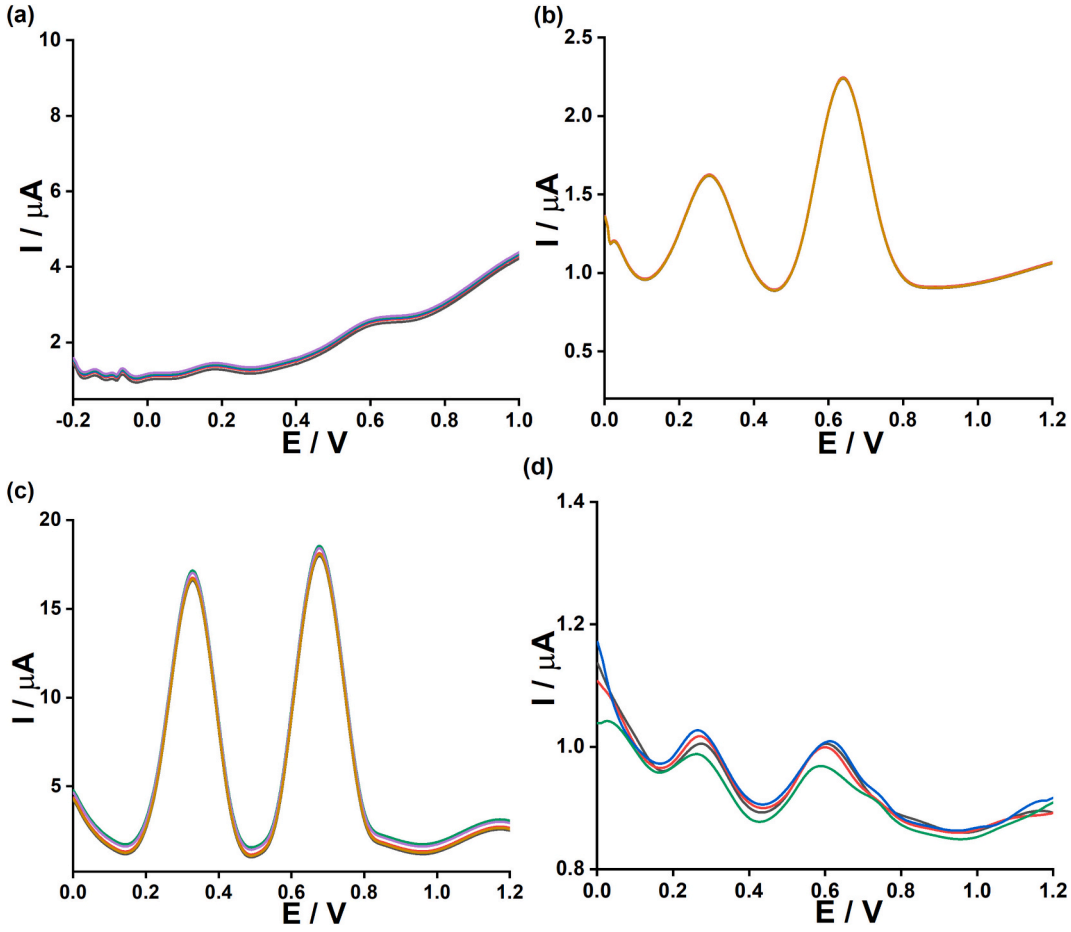

Fig. 8. DPVs of URC and XAT at 3 concentrations ($n = 6$): (a) 0.1 μM, (b) 0.19 μM, (c) 2.32 μM, and (d) 4 times of modifying GCE by PBSP-RGO in the solution included 0.1 μM of URC and XAT.

2.32 μM) in a 0.2 M PBS solution (pH 7.0). Six consecutive measurements were performed for each solution, and as illustrated in Fig. 8a-c, the resulting peak currents showed minimal variation. The calculated relative standard deviations (RSDs) were found to be 3.6 %, 2.1 %, and 1.9 % for URC, with corresponding values of 3.0 %, 2.5 %, and 2.2 % for XAT. To further validate the method's precision, these experimental RSDs were benchmarked against the theoretical limits calculated from the Horwitz equation ($RSD_{Horwitz} = 2^{1-0.5logC}$), where C is the analyte content in decimal form [34]. The experimental RSDs were all found to be less than half of the calculated Horwitz values (½.$RSD_{Horwitz}$), which were determined to be 15 %, 9.7 %, and 6.1 % for URC and 14 %, 9.1 %, and 5.7 % for XAT. This comparison describes that the PBSP-RGO/GCE electrode provides a satisfactory degree of repeatability [34].

To determine the inter-electrode consistency, the reproducibility of the fabrication method was assessed. This was achieved by preparing four independent PBSP-RGO/GCEs, each used to record the DPV response of a 0.2 M PBS solution (pH 7.0) containing 0.1 μM of both URC and XAT. The relative standard deviations (RSDs) calculated from the peak currents across these four distinct electrodes were 2.5 % for URC and 3.1 % for XAT, as depicted in Fig. 8d. Since these RSD values are well below 5 %, the consistency of the electrode modification process is verified. The stable electrochemical performance across independently prepared electrodes highlights the reliability of the sensor. This good degree of reproducibility reinforces the sensor's potential for dependable, practical use in the simultaneous electrochemical detection of URC and XAT.

Table 4
Determination results of URC and XAT in real samples by the DPV method and comparison with the reference HPLC method ($n = 3$).*

Sample	Analyte	Detected (μM)		Spiked (μM)	Detected (μM)		Rev(%)	
		DPV	HPC		DPV	HPC	DPV	HPC
Urine 1	URC	2.867	2.653	5.0	7.690	7.767	96	102
	XAT	0.122	0.183	5.0	5.188	5.125	101	99
Urine 2	URC	2.880	3.012	5.0	7.711	7.927	97	98
	XAT	0.140	0.122	5.0	5.023	5.174	98	101
Urine 3	URC	2.693	2.640	5.0	7.926	7.600	105	99
	XAT	0.160	0.169	5.0	4.976	5.057	96	98

* **Limitations and Future Perspectives:** While the PBSP-RGO/GCE sensor exhibits excellent performance for the simultaneous determination of URC and XAT, certain limitations are acknowledged. The fabrication process, although environmentally friendly, relies on electrochemical parameters that must be strictly controlled to ensure batch-to-batch reproducibility. Furthermore, while the sensor shows good anti-fouling properties in diluted urine, the long-term stability of the polymer film in continuous monitoring scenarios or highly protein-rich matrices without pretreatment remains to be fully established in future investigations.

3.4.5. Analysis of the practical samples

To evaluate the practical applicability of the developed sensor, the determination of URC and XAT was performed in five real samples using the standard addition method. For validation, the results obtained by the proposed DPV method were compared against those from a reference HPLC technique.

As presented in Table 4, satisfactory recovery rates for the DPV method were obtained, ranging from 96 % to 105 %. This result illustrates a suitable level of accuracy and reliability of the proposed sensor for the analyzed process in complex matrices. To further assess the agreement between the 02 methods, a paired *t*-test was performed on the obtained concentration values. At $\alpha = 0.05$, the statistical comparison indicated no significant difference between the results of the two techniques, URC: $t(6) = 0.327$, $p = 0.379$ (> 0.05), XAT: $t(6) = 1.178$, $p = 0.146$ (> 0.05). Therefore, it may be concluded that the developed DPV method appears to be a good reliable and effective alternative for detecting URC and XAT.

4. Conclusions

An electrochemical method for the simultaneous determination of uric acid and xanthine was developed utilizing a poly(bromocresol purple) and reduced graphene oxide composite. The application of a single-step electrochemical co-synthesis is presented as a methodological contribution, which simplifies the electrode modification process by eliminating the requirement for chemical reductants. Through the implementation of a chemometric experimental design, the synthesis parameters were optimized to address the issue of signal overlap commonly encountered with these purine metabolites.

It was observed that the prepared interface facilitates the resolution of the oxidation peaks for the target analytes. The analytical performance was evaluated, and the method was demonstrated to be applicable for the quantification of uric acid and xanthine in spiked urine samples with adequate recovery rates. The results obtained from the differential pulse voltammetry technique were found to be statistically comparable to those from high-performance liquid chromatography. These findings suggest that the proposed electro-synthesis strategy may serve as a practical alternative for developing sensing interfaces in clinical analysis.

CRediT authorship contribution statement

Nguyen Minh Quang: Software, Methodology, Data curation. **Do Mai Nguyen:** Writing – original draft, Resources, Methodology, Data curation. **Vo Chau Ngoc Anh:** Software, Resources, Methodology, Data curation. **Tran Thanh Tam Toan:** Writing – review & editing, Writing – original draft, Software, Project administration, Data curation. **Anh-Quang Dao:** Writing – review & editing, Writing – original draft, Software, Resources, Methodology.

Declaration of competing interest

The authors declare that they have no known competing financial interests or personal relationships that could have appeared to influence the work reported in this paper.

Appendix A. Supplementary data

Supplementary data to this article can be found online at https://doi.org/10.1016/j.jelechem.2026.119801.

References

[1] M. Cross, K.L. Ong, G.T. Culbreth, J.D. Steinmetz, E. Cousin, H. Lenox, J.A. Kopec, L.M. Haile, P.M. Brooks, D.R. Kopansky-Giles, K.E. Dreinhoefer, N. Betteridge, M. Abbasian, M. Abbasifard, A. Abedi, M.B. Aboye, A.Y. Aravkin, A. Artaman, M. Banach, I.M. Bensenor, A.S. Bhagavathula, A.N. Bhat, S. Bitaraf, R. Buchbinder, K. Burkart, D.T. Chu, S.C. Chung, O. Dadras, X. Dai, S. Das, S. Dhingra, T.C. Do, H. A. Edinur, A. Fatehizadeh, G. Fetensa, M. Freitas, B. Ganesan, A. Gholami, T.K. Gill, M. Golechha, P. Goleij, N. Hafezi-Nejad, S. Hamidi, S.I. Hay, S. Hundessa, H. Iso, S. Jayaram, V. Kadashetti, I.M. Karaye, E.A. Khan, M.A.B. Khan, M.M. Khatatbeh, A. Kiadaliri, M.S. Kim, A.A. Kolahi, K. Krishan, N. Kumar, T.T.T. Le, S.S. Lim, S. W. Lobo, A. Majeed, A.A. Malik, M.K. Mesregah, T. Mestrovic, E.M. Mirrakhimov, M. Mishra, A.K. Misra, M.E. Moberg, N.S. Mohamed, S. Mohan, A.H. Mokdad, K. Momenzadeh, M.A. Moni, Y. Moradi, V. Mougin, S. Mukhopadhyay, C.J. L. Murray, S.N. Swamy, V.T. Nguyen, R.K. Niazi, M.O. Owolabi, J.R. Padubidri, J. Patel, S. Pawar, P. Pedersini, Q. Rafferty, M. Rahman, M.M. Rashidi, S. Rawaf, A. M.A. Saad, A. Sahebkar, F.S. Sharif-Askari, M.A. Saleh, A.E. Schumacher, A. Seylani, P. Singh, A.E. Smith, R. Solanki, Y. Solomon, K.K. Tan, N.Y. Tat, N.S. S. Tibebu, Y. You, P. Zheng, O.A. Zitoun, T. Vos, L.M. March, A.D. Woolf, Global, regional, and national burden of gout, 1990–2020, and projections to 2050: a systematic analysis of the global burden of disease study 2021, Lancet Rheumatol. 6 (2024) e507–e517, https://doi.org/10.1016/S2665-9913(24)00117-6.

[2] M. Burnier, Gout and hyperuricaemia: modifiable cardiovascular risk factors? Front. Cardiovasc. Med. 10 (2023) 1190069.

[3] L. Zheng, Y. Zhu, Y. Ma, H. Zhang, H. Zhao, Y. Zhang, Z. Yang, Y. Liu, Relationship between hyperuricemia and the risk of cardiovascular events and chronic kidney disease in both the general population and hypertensive patients: a systematic review and meta-analysis, Int. J. Cardiol. 399 (2024) 131779.

[4] H. Sekizuka, Uric acid, xanthine oxidase, and vascular damage: potential of xanthine oxidoreductase inhibitors to prevent cardiovascular diseases, Hypertens. Res. 45 (2022) 772–774, https://doi.org/10.1038/s41440-022-00891-7.

[5] Y. Kotozaki, M. Satoh, T. Nasu, K. Tanno, F. Tanaka, M. Sasaki, Human plasma xanthine oxidoreductase activity in cardiovascular disease: evidence from a population-based study, Biomedicines 11 (2023) 754.

[6] Y. Li, Z. Chen, B. Xu, G. Wu, Q. Yuan, X. Xue, Y. Wu, Y. Huang, S. Mo, Global, regional, and national burden of gout in elderly 1990–2021: an analysis for the global burden of disease study 2021, BMC Public Health 24 (2024) 3298.

[7] K.C. Heydorn, X. Wu, T.J. Garrett, M. Kamat, D. Pandey, S. Vavilala, J. Dwyer, E. Wambogo, A.G. Ershow, L.D. Thompson, S.P. Juraschek, P.R. Pehrsson, USDA and ODS-NIH Database for the Purine Content of Foods Release 2.0, 2025, pp. 1–29. https://www.ars.usda.gov/northeast-area/beltsville-md-bhnrc/beltsville-human-nutrition-.

[8] J.M. Roseland, B. Wu, A.G. Ershow, K. Heydorn, C. Haggans, S.P. Juraschek, P. R. Pehrsson, USDA and ODS-NIH Database for the Purine Content of Foods (2023) 1–14.

[9] Z.-Y. Wen, Y.-F. Wei, Y.-H. Sun, W.-P. Ji, Dietary pattern and risk of hyperuricemia: an updated systematic review and meta-analysis of observational studies, Front. Nutr. 11 (2024) 1218912.

[10] P.K. Prabhakar, S. Vatsa, P.P. Srivastav, S.S. Pathak, A comprehensive review on freshness of fish and assessment: analytical methods and recent innovations, Food Res. Int. 133 (2020) 109157.

[11] Y. Wang, F. Li, X. Wang, C. Ma, Integrating hypoxanthine and K value for reliable and rapid freshness assessment in marine fish, Food Chem. 470 (2025) 142630.

[12] A. Vernerová, L. Kujovská Krčmová, B. Melichar, F. Švec, Non-invasive determination of uric acid in human saliva in the diagnosis of serious disorders, Clin. Chem. Lab. Med. 59 (2021) 797–812.

[13] S.-H. Han, K.W. Moon, Y.J. Lee, G.-J. Lee, Simultaneous electrochemical analysis of uric acid and xanthine in human saliva and serum samples using a 3D reduced graphene oxide nanocomposite-modified electrode, Chemosensors 11 (2023) 185.

[14] M.A. Raj, S.A. John, Simultaneous determination of uric acid, xanthine, hypoxanthine and caffeine in human blood serum and urine samples using electrochemically reduced graphene oxide modified electrode, Anal. Chim. Acta 771 (2013) 14–20.

[15] L. Chen, Y. Tang, K. Wang, C. Liu, S. Luo, Direct electrodeposition of reduced graphene oxide on glassy carbon electrode and its electrochemical application, Electrochem. Commun. 13 (2011) 133–137.

[16] A. Zhou, J. Bai, W. Hong, H. Bai, Electrochemically reduced graphene oxide: preparation, composites, and applications, Carbon N. Y. 191 (2022) 301–332.

[17] F. Cui, X. Zhang, A method based on electrodeposition of reduced graphene oxide on glassy carbon electrode for sensitive detection of theophylline, J. Solid State Electrochem. 17 (2013) 167–173.

[18] Y. Wang, L. Tong, Electrochemical sensor for simultaneous determination of uric acid, xanthine and hypoxanthine based on poly (bromocresol purple) modified glassy carbon electrode, Sens. Actuators B 150 (2010) 43–49.

[19] S. Koçak, B. Aslışen, Hydrazine oxidation at gold nanoparticles and poly (bromocresol purple) carbon nanotube modified glassy carbon electrode, Sens. Actuators B 196 (2014) 610–618.

[20] S. Koçak, B. Aslışen, Ç.C. Koçak, Determination of hydrazine at a platinum nanoparticle and poly (bromocresol purple) modified carbon nanotube electrode, Anal. Lett. 49 (2016) 990–1003.

[21] X. Zhu, J. Liu, Z. Zhang, N. Lu, X. Yuan, D. Wu, Green synthesis of a bromocresol purple/graphene composite and its application in electrochemical determination of 2, 4, 6-trichlorophenol, Anal. Methods 7 (2015) 3178–3184.

[22] X. Liu, J. Dai, J. Shen, D. Zhu, K. Rajalakshmi, S. Muthusamy, T. Kanagaraj, P. Kannan, Simultaneous and selective determination of purine metabolites in human urine samples using nanocomposite modified glassy carbon electrode, J. Mol. Liq. 411 (2024) 125845.

[23] A.G. Marrani, A. Motta, R. Schrebler, R. Zanoni, E.A. Dalchiele, Insights from experiment and theory into the electrochemical reduction mechanism of graphene oxide, Electrochim. Acta 304 (2019) 231–238.

[24] S.Y. Toh, K.S. Loh, S.K. Kamarudin, W.R.W. Daud, The impact of electrochemical reduction potentials on the electrocatalytic activity of graphene oxide toward the

oxygen reduction reaction in an alkaline medium, Electrochim. Acta 199 (2016) 194–203.
[25] F.C. Moraes, R.G. Freitas, R. Pereira, L.F. Gorup, A. Cuesta, E.C. Pereira, Coupled electronic and morphologic changes in graphene oxide upon electrochemical reduction, Carbon N. Y. 91 (2015) 11–19, https://doi.org/10.1016/j.carbon.2015.04.038.
[26] A. Safaei, S. Sadeghi, A new electrochemical sensor for the detection of uric acid and xanthine based on a carbon paste electrode coated with a metal organic framework, Anal. Methods 17 (2025) 6405–6419, https://doi.org/10.1039/D5AY00832H.
[27] K. Hayat, A. Munawar, A. Zulfiqar, M.H. Akhtar, H.B. Ahmad, Z. Shafiq, M. Akram, A.S. Saleemi, N. Akhtar, CuO hollow cubic caves wrapped with biogenic N-rich graphitic C for simultaneous monitoring of uric acid and xanthine, ACS Appl. Mater. Interfaces 12 (2020) 47320–47329, https://doi.org/10.1021/acsami.0c15243.
[28] M.W. Ahmad, B. Dey, G. Sarkhel, D.-J. Yang, A. Choudhury, Sea-urchin-like cobalt-MOF on electrospun carbon nanofiber mat as a self-supporting electrode for sensing of xanthine and uric acid, J. Electroanal. Chem. 920 (2022) 116646, https://doi.org/10.1016/j.jelechem.2022.116646.
[29] N. Sudhan, S. Anitta, S. Meenakshi, C. Sekar, Brushite nanoparticles based electrochemical sensor for detection of uric acid, xanthine, hypoxanthine and caffeine, Anal. Biochem. 659 (2022) 114947, https://doi.org/10.1016/j.ab.2022.114947.
[30] J.M. Mohan, K. Amreen, A. Javed, S.K. Dubey, S. Goel, Highly selective electrochemical sensing of dopamine, xanthine, ascorbic acid and uric acid using a carbon Fiber paper, IEEE Sensors J. 20 (2020) 11707–11712, https://doi.org/10.1109/JSEN.2020.2999067.
[31] B. Dey, M.W. Ahmad, G. Sarkhel, G. Ho Lee, A. Choudhury, Fabrication of niobium metal organic frameworks anchored carbon nanofiber hybrid film for simultaneous detection of xanthine, hypoxanthine and uric acid, Microchem. J. 186 (2023) 108295, https://doi.org/10.1016/j.microc.2022.108295.
[32] S. Yu, Z. Yue, X. Wang, S. Zhang, Z. Zhou, L. Zhang, Y. Ma, PTA/CeO2@Pt-based electrochemical sensors to detect xanthine and uric acid, and evaluate fish freshness, Chem. Eng. J. 490 (2024) 151646, https://doi.org/10.1016/j.cej.2024.151646.
[33] M. Li, Z. Ma, T. Zhang, W. Wang, L. Xue, D. Zhu, Boron/nitrogen co-doped reticulated porous carbon frameworks encapsulating cobalt selenide: an advanced nanomaterial for ultrasensitive simultaneous detection of xanthine and uric acid in human serum, Microchem. J. 218 (2025) 115188, https://doi.org/10.1016/j.microc.2025.115188.
[34] W. Horwitz, R. Albert, Quality IssuesThe concept of uncertainty as applied to chemical measurements, Analyst 122 (1997) 615–617.